Theoretical Investigation of Monolayer RhTeCl Semiconductors as Photocatalysts for Water Splitting

Yiran Ying[a+], *Ke Fan*[a+], *Sicong Zhu*[ab+], *Xin Luo*[c]*, *and Haitao Huang*[a]*

[a] Department of Applied Physics, The Hong Kong Polytechnic University, Hung Hom, Kowloon, Hong Kong, P.R. China

[b] College of Science and Key Laboratory for Ferrous Metallurgy and Resources Utilization of Ministry of Education, Wuhan University of Science and Technology, Wuhan 430065, P.R. China

[c] School of Physics, Sun Yat-sen University, Guangzhou, Guangdong Province, P.R. China, 510275

AUTHOR INFORMATION

Corresponding Author

*E-mail: luox77@mail.sysu.edu.cn; aphhuang@polyu.edu.hk.

[+]These authors contribute equally to this work.

ABSTRACT.

Photocatalytic water splitting, an environmentally friendly approach for producing hydrogen, is a feasible and efficient solution for the environmental and energy crisis. A major challenge for photocatalytic water splitting is searching for catalysts with suitable band gap and band alignment with promising electronic and optical properties. Herein, we predict a novel two-dimensional material, monolayer RhTeCl, which is potentially exfoliable from its bulk counterparts with a small cleavage energy (~0.39 J/m^2). Dynamical, thermal, and mechanical stabilities, as well as suitable direct band gap (2.49 eV) and band edge positions qualify monolayer RhTeCl as a promising candidate for photocatalytic water splitting. High electron mobility and exciton binding energy further suppress the electron-hole recombination, and good light harvesting ability is presented with pronounced optical absorbance in the visible light and ultraviolet regions. In addition, the Gibbs free energy diagram shows that water splitting on monolayer RhTeCl can be effectively driven by solar energy. These features render monolayer RhTeCl semiconductors as promising photocatalysts for water splitting.

1. Introduction

Photocatalytic water splitting into hydrogen (H_2) and oxygen (O_2) with the help of solar energy, has become a promising environmentally friendly approach for hydrogen production and energy conversion since the pioneering work by Fujishima and Honda in 1972.[1] Three steps are usually identified in the photocatalytic water splitting process: charge carriers generation induced by excitons, charge separation and transfer, and hydrogen evolution reaction (HER) and oxygen evolution reaction (OER) on the catalyst surface.[2-3] The efficiency of photocatalytic water splitting is greatly determined by the performance of photocatalysts in the abovementioned steps. An ideal photocatalyst should satisfy several conditions. First, the band gap of an ideal photocatalyst should be larger than the thermodynamic potential of water splitting (1.23 eV), but smaller than 3.0 eV in order to utilize solar energy of visible light efficiently.[4-6] Second, the band edges should be at the right potentials to drive the redox reactions, which means that the conduction band minimum (CBM) of the photocatalyst should be higher than -4.44 eV (reduction potential of H^+/H_2) and the valence band maximum (VBM) should be lower than -5.67 eV (oxidation potential of O_2/H_2O).[6-7] Third, photocatalysts should have small exciton binding energy and low exciton recombination rate, separate carriers efficiently, and transfer carriers rapidly to avoid surface charge recombination.[6] Unfortunately, the low efficiency hinders the mass applications of the currently available photocatalysts. Therefore, searching for novel photocatalysts for water splitting has become a major challenge.

Among all types of photocatalysts, two-dimensional (2D) materials stand out for the following two reasons. On the one hand, 2D materials have large surface area and a high portion of exposed active sites for enhancing surface photochemical reactions. On the other hand, reduced carrier migration distance caused by the ultrathin nature of 2D materials can greatly enhance the carrier

separation, benefiting the photocatalysis process. These advantages make 2D semiconductors with suitable band gap ranging from 1.5 to 3.0 eV attractive candidates for photocatalytic water splitting.[3, 8] Theoretical calculation has been a powerful tool in designing novel 2D photocatalysts for water splitting[6, 9], and recent examples include, but not limited to, $MnPSe_3$[10], GeS/GeSe[11], GeTe[12], $PdSeO_3$[7], $Pd_3P_2S_8$[13], Janus MoSSe[14-15], $Pd_3(PS_4)_2$[16], SiP_2[17], Janus PtSSe[18], and penta-X_2C (X=P, As, Sb)[19]. Nevertheless, the difficulty in the experimental realization urges more theoretical work into this burgeoning area.

In 2018, Mounet and coworkers identified 1,825 compounds which are easily or potentially easily exfoliable from their 3D counterparts by using high-throughput computations.[20] Their work provided pioneer guidance for searching possible 2D photocatalysts for water splitting. Among those compounds, we identify one compound, RhTeCl, as a potential candidate. It has a direct band gap of 1.1 eV as estimated by Perdew-Burke-Ernzerhof (PBE) functional,[20] which usually underestimates the exact band gap values.[21] The exact band gap value of monolayer RhTeCl may satisfy the requirements for water splitting photocatalysts. Köhler et al. obtained the three-dimensional rhodium chalcogenide halide (RhTeCl) crystals by chemical transport reaction in 1997.[22] We also note a recent publication in which monolayer RhTeCl field-effect transistors were simulated by using quantum transport approaches.[23] However, a comprehensive study of the properties and potential applications of monolayer RhTeCl in photocatalytic water splitting has not yet been conducted theoretically or experimentally.

In this work, we systematically investigate the stabilities as well as the structural, elastic, electronic, transport, and optical properties of monolayer RhTeCl by density functional theory (DFT), ab initio molecular dynamics (AIMD), and non-equilibrium Green's function (NEGF) calculations. Results show that monolayer RhTeCl has dynamical, thermal, and mechanical

stabilities and a direct band gap of 2.49 eV. In addition, the aligned band edge (CBM at -4.01 eV and VBM at -6.50 eV) also satisfies the requirement for water splitting photocatalysts. The outstanding carrier transport and optical properties can effectively suppress the electron-hole recombination in the photocatalysis, together with outstanding water splitting thermodynamics, which make monolayer RhTeCl an ideal candidate for photocatalytic water splitting.

2. Computational Methods

First-principles density functional theory (DFT) calculations were performed by using projector-augmented wave method implemented in the Vienna ab initio Simulation Package (VASP)[24-25]. The PBE flavor of the generalized gradient approximation[26] was applied for the exchange-correlation functional. 4*p*5*s*4*d*, 5*s*5*p*, and 3*s*3*p* electrons were considered as valence electrons for Rh, Te, and Cl. Kinetic energy cut-off was set as 450 eV in all calculations. Energy and force convergence criteria were set as 1×10^{-5} eV and 0.02 eV/Å, respectively. The meshes of Monkhorst-Pack *k*-points sampling[27] for the calculations of unit cell and 2×2×1 supercell were set as 17×7×1 and 5×3×1, respectively. Vacuum layer with a thickness of 20 Å was used to avoid spurious interactions between adjacent image cells. For the band structures and band alignment calculations, a more sophisticated HSE06 hybrid functional with the fraction of local exact exchange of 0.25[28-29] was used. Grimme's DFT-D3 scheme[30] was applied to account for the van der Waals interactions during the calculations. Crystal structures and electron localized function (ELF) were visualized with the Visualization for Electronic and Structural Analysis (VESTA) version 3.[31]

Phonon dispersion spectra were calculated by using the density functional perturbation theory (DFPT) implemented in the PHONOPY code[32] interfaced with VASP with the local density approximation functionals. During phonon dispersion calculation, energy and force convergence

criteria were set as 1×10^{-8} eV and 0.001 eV/Å, respectively, and a 3×3×1 supercell was used. *Ab initio* molecular dynamics (AIMD) simulations were performed in the NVT (canonical) ensemble with Nosé-Hoover thermostat[33-34], and 2×2×1 supercell was applied in the simulations. The quantum transport characteristics were simulated by combining NEGF with DFT (details can be found in the Supporting Information)[35-37].

For the optical spectra calculations, the excitonic effect was included through solving the Bethe-Salpeter equation (BSE)[38-39] with Tamm-Dancoff approximation[40] on top of single-shot GW (G_0W_0). Γ-centered 6×6×1 grid was used for *k*-points sampling during the GW and BSE calculations, and the energy cut-off values for the plane-wave basis and response function were 400 and 150 eV, respectively. Absorption coefficient α(ω) was given by the following equation:

$$\alpha(\omega) = \sqrt{2}\omega[\sqrt{\varepsilon_1(\omega)^2 + \varepsilon_2(\omega)^2} - \varepsilon_1(\omega)]^{1/2}$$

where $\varepsilon_1(\omega)$ and $\varepsilon_2(\omega)$ represent real and imaginary parts of the frequency-dependent dielectric function, respectively.

The adsorption energy of adsorbate on a substrate was calculated using the formula:

$$E_{ads}=E(total)-E(substrate)-E(adsorbate)$$

where E(substrate), E(adsorbate), and E(total) represent DFT-calculated total energies of the substrate, the adsorbate, and the system including both, respectively. Gibbs free energy changes for all intermediates in HER and OER were calculated as:[41]

$$\Delta G=\Delta E_{DFT}+\Delta E_{ZPE}-T\Delta S+\Delta G_{pH}$$

where ΔE_{DFT}, ΔE_{ZPE}, $T\Delta S$, and ΔG_{pH} represent the difference of DFT-calculated adsorption energy, zero point energy (ZPE), entropic contribution, and free energy correction of pH in each reaction step. Gibbs free energy for $H^+ + e^-$ was calculated through the conventional hydrogen electrode (CHE) model to simulate the anode reaction ($H_2 \rightleftarrows 2(H^+ + e^-)$):[42]

$$G(H^+ + e^-) = 0.5G(H_2) - eU$$

where U represents the electrode potential relative to the CHE.

3. Results and Discussions

3.1 Geometric structure and stabilities of monolayer RhTeCl

The relaxed geometric structure of 2D RhTeCl is plotted in Figure 1 and it possesses the space group $P2_1/m$ (No. 11). The geometric structure of monolayer RhTeCl is similar to that of transition metal dichalcogenides in the 1T phase and the Rh layer is sandwiched between two layers of nonmetal atoms, with half of the Te atoms in the $RhTe_2$ replaced by Cl atoms along x-axis (Figure 1a). Each Rh atom is coordinated by three Te and three Cl atoms and forms edge-shared octahedra. The lattice constants which are optimized with PBE functional and DFT-D3 correction are a=3.67 Å, b=6.65 Å, which is very close to experimental values for bulk RhTeCl (a=3.64 Å, b=6.65 Å, c=12.99 Å)[22], confirming the validity of our calculations.

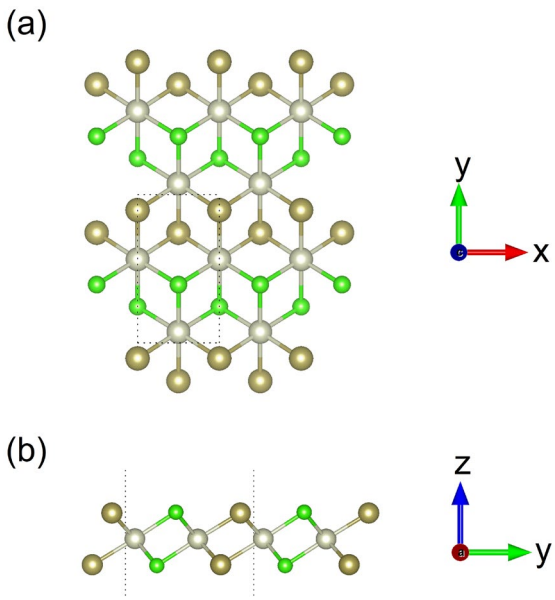

Figure 1. (a) Top and (b) side view of the geometric structure of monolayer RhTeCl. Dotted lines denote the boundaries of the unit cell. Rh, Te, and Cl atoms are represented by grey, brownish yellow, and green balls, respectively.

Before we move on to other properties, the stabilities of 2D RhTeCl must be examined. The phonon dispersion spectrum calculated by DFPT is shown in Figure 2a. It manifests that the low-frequency optical and acoustic branches are well separated from each other near the Γ point, and no imaginary frequencies can be seen in the entire Brillouin zone except for small ones in the transverse acoustical phonon branch near the Γ point, which can be attributed to the artifacts of numerical calculations.[43-44] This indicates that monolayer RhTeCl is dynamically stable.

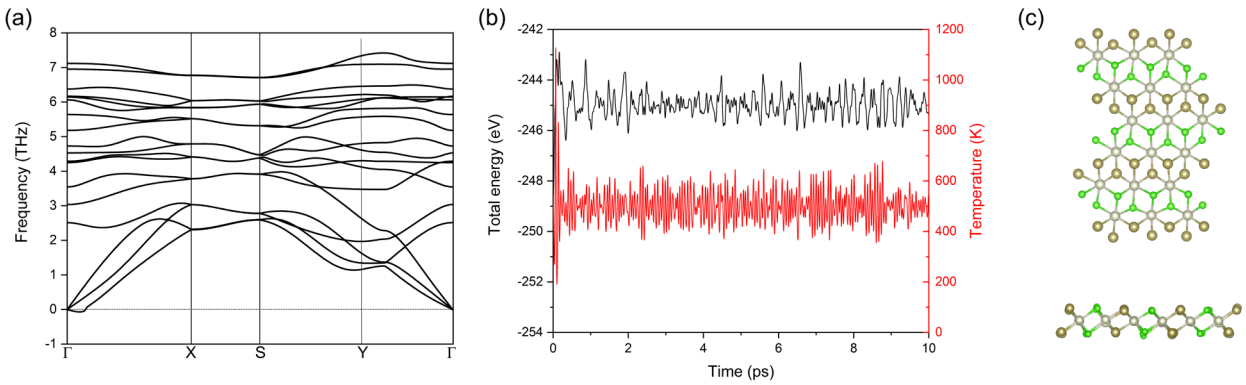

Figure 2. (a) Phonon dispersion spectra of monolayer RhTeCl. Brillouin zone path is set as Γ(0,0,0)→X(0.5,0,0)→S(0.5,0.5,0)→Y(0,0.5,0)→Γ. (b) Total energy and temperature as a function of time during AIMD simulation of RhTeCl 2×2×1 supercell under 500 K, and (c) top and side views of the snapshot of monolayer RhTeCl after 10 ps in AIMD simulation.

To check the thermal stability of monolayer RhTeCl, we perform AIMD simulation with NVT ensemble under the temperature of 500 K for 10 ps. During the simulation, the total energy and

temperature reach their equilibrium values quickly and then oscillate around them, and a snapshot of the geometric structure after the simulation shows no obvious structural reconstruction (Figure 2c). After the simulation, the pristine structure can be recovered by geometric relaxation again. This suggests that monolayer RhTeCl is thermally stable.

Two-dimensional elastic constants are obtained from renormalization by multiply the thickness of vacuum layer with three-dimensional elastic constants[45] which are obtained from the strain-stress relations[46]. For simplicity, we use the conventional standard cell in the calculations, and only four elastic constants (C_{11}, C_{12}, C_{22}, and C_{66} in the Voigt notation 1-xx, 2-yy, and 6-xy[47]) are independent, with values of C_{11}=51.78 N/m, C_{12}=12.88 N/m, C_{22}=45.83 N/m, and C_{66}=15.14 N/m. The Born criteria ($C_{11}C_{22}$-C_{12}^2>0, C_{66}>0)[48] are satisfied, indicating that monolayer RhTeCl is mechanically stable. In addition, we calculate the orientation-dependent Young's modulus Y(θ) and Poisson's ratio ν(θ) (θ is the angle with respect to the x axis) using the following formula:[49-50]

$$Y(\theta) = \frac{D}{C_{22}\cos^4\theta + \left(\frac{D}{C_{66}} - 2C_{12}\right)\cos^2\theta\sin^2\theta + C_{11}\sin^4\theta}$$

$$\upsilon(\theta) = \frac{C_{12}\cos^4\theta - \left(C_{11} + C_{22} - \frac{D}{C_{66}}\right)\cos^2\theta\sin^2\theta + C_{12}\sin^4\theta}{C_{22}\cos^4\theta + \left(\frac{D}{C_{66}} - 2C_{12}\right)\cos^2\theta\sin^2\theta + C_{11}\sin^4\theta}$$

here, $D = C_{11}C_{22} - {C_{12}}^2$. As shown in Figure 3a and 3b, Young's moduli reach the maximum values at θ=0°, and minimum ones at θ=45°. Poisson's ratios, on the other hand, reach the minimum along the x direction and maximum along the y direction (θ=90°). The angular dependences of Young's modulus and Poisson's ratio indicate mechanical anisotropy of monolayer RhTeCl. It is interesting to notice that Young's modulus of monolayer RhTeCl (32.8-48.2 N/m) is far smaller than some typical 2D materials such as graphene (342 N/m)[47] and MoS_2 (129 N/m)[51], indicative of the fact that RhTeCl is less rigid than these materials.

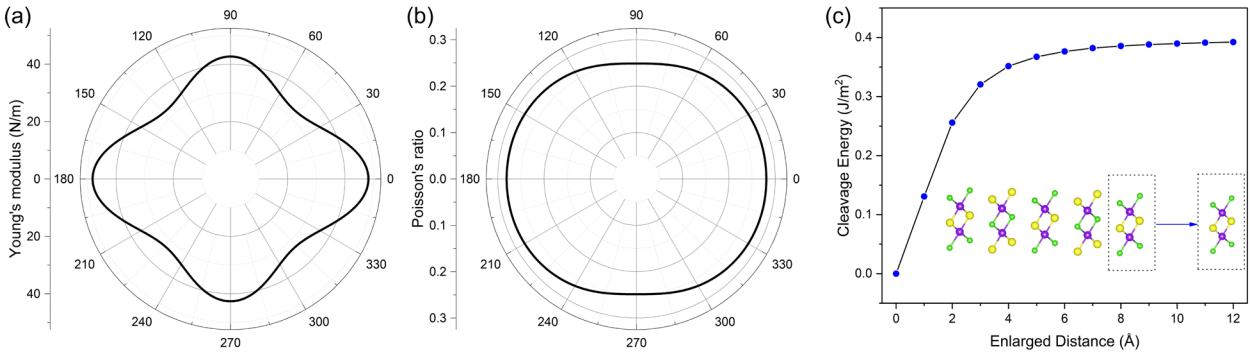

Figure 3. Orientation-dependent (a) Young's modulus and (b) Poisson's ratio for monolayer RhTeCl. (c) Cleavage energy as a function of enlarged distance for RhTeCl (inset shows the schematic illustration of the modeling in the cleavage energy calculations).

A useful way of experimental synthesis of 2D materials is the mechanical or liquid exfoliation of their bulk counterparts.[52-54] Here, we check the feasibility of the experimental exfoliation of 2D RhTeCl by calculating its cleavage energy. We first construct a structure containing a quintuple layer of RhTeCl and then remove the first layer away from the others over a certain distance. We calculate the cleavage energy as a function of the enlarged distance, as shown in Figure 3c. The cleavage energy gradually increases with increased distance and converges to the value of 0.39 J/m^2. This value is very close to that of graphene (~0.37 J/m^2)[52, 55], and is lower than some experimentally exfoliable 2D materials, including GeS (~0.52 J/m^2)[56-57] and Ca_2N (~1.09 J/m^2)[58-59]. Therefore, we expect that bulk RhTeCl will also be exfoliated either mechanically or chemically down to monolayers.

3.2 Electronic, carrier transport, and optical properties of monolayer RhTeCl

Next, we examine the electronic properties of monolayer RhTeCl. We first consider the influence of spin-orbit coupling (SOC) effect. As shown in Figure S1, the band structures with and without considering SOC are very similar and the band gap values calculated by PBE and PBE+SOC are 1.14 and 1.11 eV, respectively, indicating that SOC effect does not have a significant influence on the electronic structures of monolayer RhTeCl. Since PBE functional seriously underestimates the exact band gap values, we use HSE06 hybrid functional to obtain more precise band structure, as shown in Figure 4. Both PBE and HSE06 functionals give direct band gap at Y point, and the band gap is 2.49 eV under HSE06, which is far larger than that under PBE and satisfies the requirement for photocatalysts (1.23-3.0 eV). Analysis of density of states (DOS) shows that VBM and CBM are mainly contributed by the Rh 4*d* orbital with small contributions from the Te 5*p* and Cl 3*p* orbitals. It is also noteworthy that the valence band near VBM (Y point) is very flat, together with the *d*-*p* and inter *p* orbital hybridization, resulting in large DOS in the vicinity of VBM (Figure 4), which benefits the light adsorption ability of monolayer RhTeCl.[60] We further use the electron localization function (ELF) to analyze the bonding characters of monolayer RhTeCl (Figure S2). ELF with the values of 1 and 0.5 show covalent bond character (electrons fully localized) and metallic bond character (electrons fully delocalized), respectively, while ELF close to zero shows ionic bond character and low charge density.[61] From Figure S2, we can conclude that Rh and Cl form strong ionic bonds (ELF~0.1), while Rh and Te form weak ionic bonds (ELF~0.25).

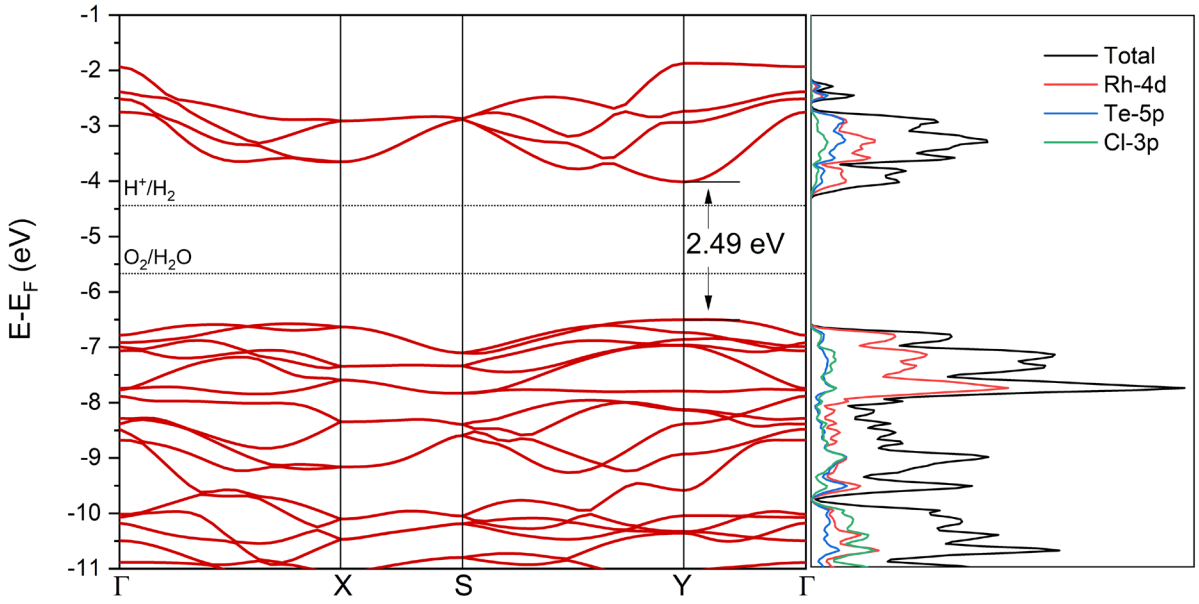

Figure 4. Band structure (left) and corresponding total and partial density of states (right) of monolayer RhTeCl calculated by HSE06 functional with vacuum level correction. Dotted lines denote water redox potential levels.

To assess whether the band edges of monolayer RhTeCl satisfy the redox potential, we further align the band edge position by considering the vacuum level corrections. The vacuum level of 2.78 eV under HSE06 is used as zero reference to locate the VBM and CBM at -6.50 eV and -4.01 eV, respectively. Since the CBM is higher than the hydrogen reduction potential (-4.44 eV) and the VBM is lower than the hydrogen oxidation potential (-5.67 eV), the thermodynamic requirement for overall water splitting is fulfilled (Figure 4). We further calculate the potential of photogenerated electrons for hydrogen reduction (U_e) and holes for water oxidation (U_h).[7] U_e, defined as the difference between CBM and the hydrogen reduction potential divided by electron charge, is 0.43 V at pH=0; U_h, on the other hand, is calculated to be 2.06 V as the difference between VBM and the hydrogen reduction potential. Considering the pH dependence of band

positions under the CHE model (0.059×pH)[7], we get the pH dependence of those potentials as U_e=0.43+0.059×pH and U_h=2.06-0.059×pH, and under neutral environment (pH=7), U_e and U_h are 0.84 V and 1.65 V, respectively, which can provide considerable driving force for both HER and OER.

External strain engineering is an important way to tune the band gap and band edge alignment for photocatalysts.[6, 9, 12-13, 16] Our results (Figure S3) show that biaxial strain can effectively modulate the band edge positions for monolayer RhTeCl, and under the biaxial strain from -5% (compression) to 4% (tensile), the band edge positions can still satisfy the requirements for photocatalytic water splitting. The band gap value also varies with strain, and to be specific, decreases under tensile strain and increases under compressive one.

We evaluate the carrier mobility μ by the deformation potential theory:[62]

$$\mu = \frac{e\hbar^3 C_{2D}}{k_B T m^* m_d (E_1)^2}$$

where C_{2D}, m^*, E_1 represent 2D elastic modulus, the carrier (electron/hole) effective mass along the transport direction, and the deformation potential constant, $m_d = \sqrt{m_x{}^* m_y{}^*}$ is the average effective mass, the temperature T is considered as 300 K, and E_1 is defined as $E_1 = \frac{\Delta E}{\Delta l / l_0}$ (ΔE, Δl, and l_0 denote the energy change of the band after deformation, the deformation of the lattice constant, and the equilibrium lattice constant, respectively). Results are all summarized in Table 1. We can conclude that the electron mobility is two orders of magnitude higher than the hole mobility along both x and y directions, remarkably facilitating the separation of electrons and holes during the photocatalysis and suppressing the electron-hole recombination. Furthermore, the electron mobility is highly anisotropic, and the value of electron mobility along y direction (420.56 $cm^2\ V^{-1}\ s^{-1}$) is higher than many 2D semiconductors such as MoS_2 (~200 $cm^2\ V^{-1}\ s^{-1}$)[63] and

comparable to many recently reported 2D photocatalysts, such as Janus MoSSe (530 and 490 $cm^2 V^{-1} s^{-1}$ along x and y directions)[14] and $Pd_3P_2S_8$ (26 and 19 $cm^2 V^{-1} s^{-1}$ along x and y directions)[13].

Table 1. 2D elastic modulus C_{2D}, carrier effective mass m^*, deformation potential E_1, and carrier mobility μ for monolayer RhTeCl.

Carrier type	C_{2D} (N/m)	m^*/m_0	E_1 (eV)	μ ($cm^2 V^{-1} s^{-1}$)
Electron (x)	51.78	2.12	2.60	84.95
Electron (y)	45.83	0.28	3.28	420.56
Hole (x)	51.78	18.1	2.80	0.76
Hole (y)	45.83	5.72	4.27	0.92

In field effect transistor (FET) devices, high carrier mobility usually produces large drain current and anisotropic materials also produce different current characteristics. To further prove the high carrier mobility of monolayer RhTeCl, we use the NEGF calculations to simulate the transport properties of monolayer RhTeCl. Because of the anisotropy of carrier mobility in monolayer RhTeCl, a transport model is established for two directions: one with the current flow in the x direction (denoted as device 1, as shown in Figure S4a), and the other with current flow in the y direction (denoted as device 2, as shown in Figure S5). Strong anisotropy of currents along y and x directions can be concluded from the I-V curve (Figure S4b) , and according to the transmission spectra (Figure S4c), the conductance channels along the y direction are larger (detailed analysis can be found in the Supporting Information below Figure S5), which is consistent with our carrier mobility calculations. Such comparatively large drain current differences in pure RhTeCl materials without chemical adsorption or doping qualify them as superior conductors, which is beneficial to

the fast transfer of electrons to the surface of catalysts during the photocatalysis and the occurrence of redox reactions.

We also calculate the optical absorbance to investigate the light harvesting performance of monolayer RhTeCl. By applying the GW+BSE approach, we predict more accurate optical absorbance spectra (Figure 5) by accounting for the excitonic effect (electron-hole interaction) while calculating the frequency-dependent dielectric function.[64-65] From Figure 5, we can conclude that optical absorbance of monolayer RhTeCl is highly anisotropic, and pronounced light absorption covering the visible and ultraviolet regions along both x and y directions. The absorption coefficient with the level of magnitude of 10^5 cm^{-1} is comparable to hybrid perovskite solar cells,[66] indicating the good light harvesting ability of monolayer RhTeCl. The exciton binding energy is about 0.45 eV which is determined by the difference of optical band gap calculated with and without considering the excitonic effect. The considerable excitonic binding energy can avoid the electron-hole recombination. To sum up, the optical properties of monolayer RhTeCl semiconductors further ensure it as good photocatalysts for water splitting.

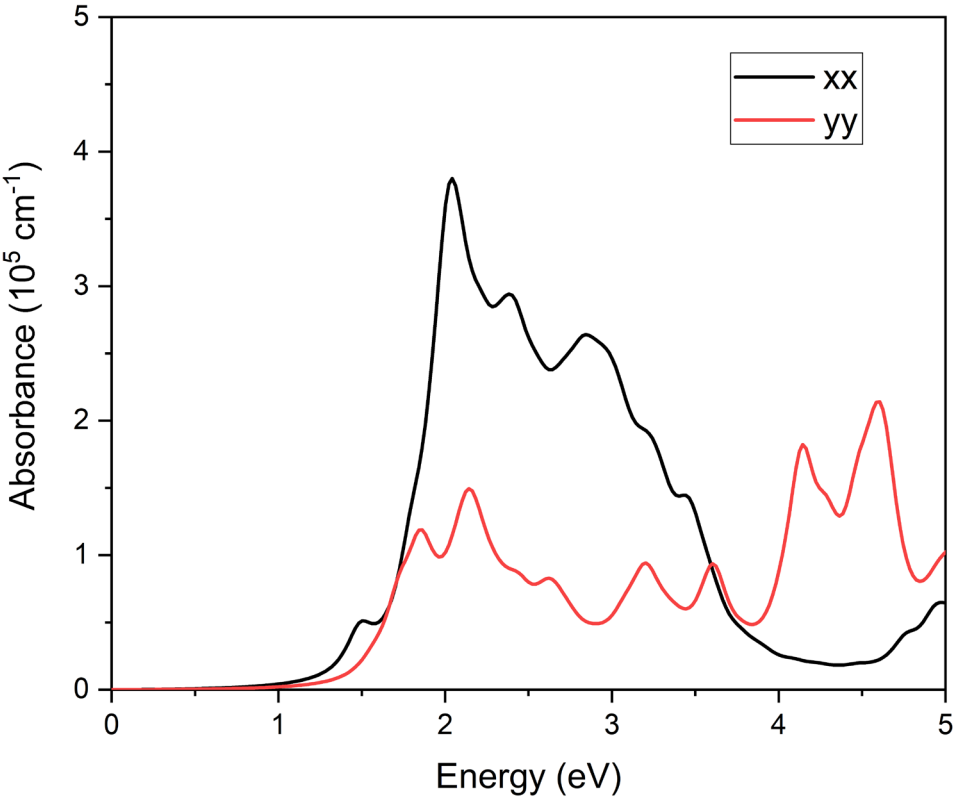

Figure 5. Optical absorbance of monolayer RhTeCl along x and y directions calculated using the GW+BSE approach.

3.3 Overall water splitting thermodynamics

In the final part, we aim to analyze the photocatalytic water splitting on monolayer RhTeCl from the perspective of thermodynamics. The OER is considered as a four proton and coupled electron transfer (PCET) process:[67]

$$*+H_2O \rightarrow *OH+H^++e^-$$

$$*OH \rightarrow *O+ H^++e^-$$

$$*O+H_2O \rightarrow *OOH+H^++e^-$$

$$*OOH \rightarrow O_2+H^++e^-$$

where * denotes active sites on the surface of the photocatalyst. We identify the active site with the lowest adsorption energy of *OH and the DFT-optimized structures of all intermediates are plotted in Figure 6. Particularly, we calculate the Gibbs free energies for all intermediates in the OER by adding the zero point energy and entropic contributions to the DFT-calculated adsorption energies (Table S1). From the Gibbs free energy diagram shown in Figure 6, we can conclude that all four steps during OER are exothermic and the potential determining step with the largest energy barrier is *O→*OOH (1.55 eV). This energy barrier can be successfully driven by the potential of photogenerated holes (U_h) under pH=7 (1.65 V) during the photocatalysis so the solar-driven oxygen evolution on monolayer RhTeCl is spontaneous. The theoretical overpotential is subsequently defined from the maximum Gibbs free energy change:[67]

$$\eta = \max[\Delta G]/e - 1.23\ [V]$$

In this context, a low theoretical overpotential of 0.32 V can be determined for monolayer RhTeCl, indicating outstanding OER activity. This value is lower than that on some literature-reported OER catalysts such as well-established $(10\bar{1}4)$ surface of β-CoOOH (0.48 V)[67] and Mn supported on C_2N monolayer (0.67 V)[68]. In addition, the barrier in HER is calculated to be 1.14 eV (Figure S6), which can be partially overcome by the potential of photogenerated electrons (0.84 eV). With effective hydrogen evolution co-catalysts to lower the activation energy by 0.30 eV or above, the photocatalytic overall water splitting on monolayer RhTeCl can be thermodynamically spontaneous.

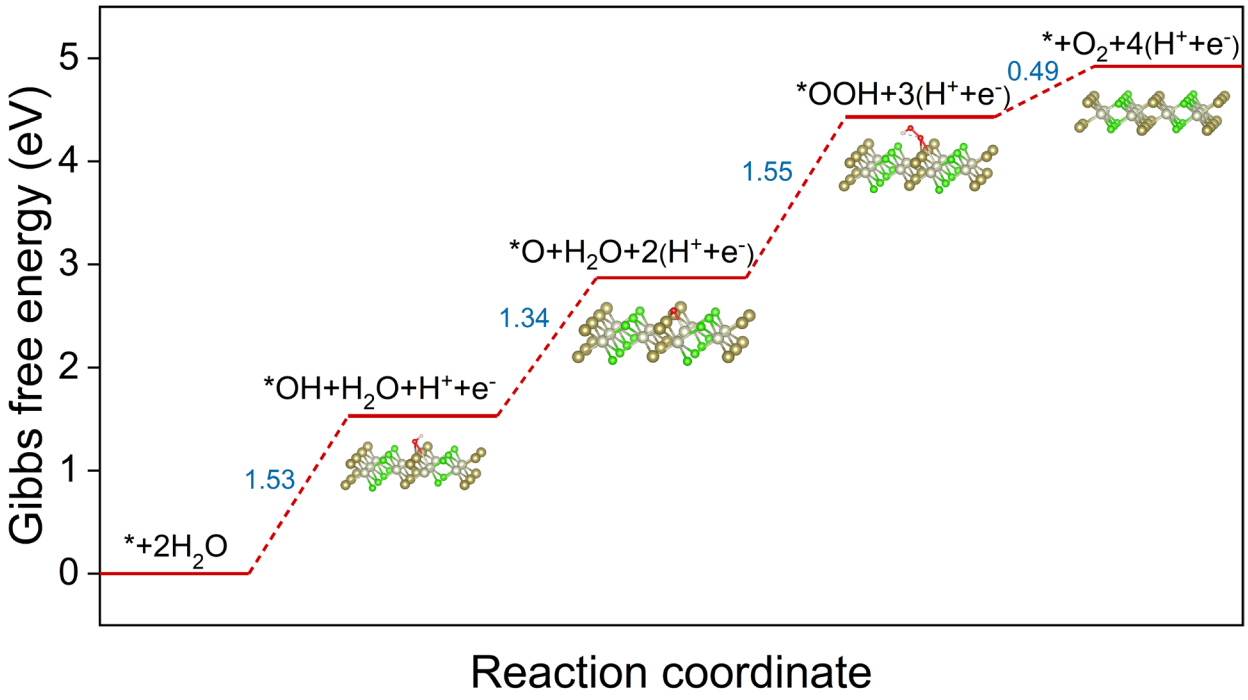

Figure 6. Gibbs free energy diagram for the oxygen evolution reaction on monolayer RhTeCl at zero potential U. DFT-optimized structures of all intermediates are also shown (Grey: Rh; brownish yellow: Te; green: Cl; red: O; pink: H). Relative Gibbs free energy change values for each step are marked and shown in eV.

4. Conclusions

In this work, we predict a novel two-dimensional material, monolayer RhTeCl, which can be potentially exfoliated from its bulk counterparts. Monolayer RhTeCl is dynamically, thermally, and mechanically stable with a direct band gap of 2.49 eV calculated with HSE06 functional, together with the aligned band edge positions, satisfying the requirements for water splitting photocatalysts. The electron mobility of monolayer RhTeCl is far higher than the hole mobility, effectively suppressing the electron-hole recombination during the photocatalysis. Moreover, the optical absorbance shows that pronounced light harvesting ability in the visible and ultraviolet regions for monolayer RhTeCl. In addition, the low theoretical OER overpotential of 0.32 V

facilitates the solar-driven water oxidation process. These features indicate that monolayer RhTeCl semiconductors have potential applications as water splitting photocatalysts.

ASSOCIATED CONTENT

Supporting Information.

The following files are available free of charge.

Details of the non-equilibrium Green's function calculations and Gibbs free energy calculations in the OER; Band structure of monolayer RhTeCl by PBE functional with and without considering SOC; Electron localized function; Band edge positions and band gap values as a function of biaxial strain; Gibbs free energy diagram for HER on RhTeCl (PDF)

AUTHOR INFORMATION

Corresponding Author

*E-mail: xin.xi.luo@polyu.edu.hk (X.L.); aphhuang@polyu.edu.hk (H.H.).

Author Contributions

The manuscript was written through contributions of all authors. All authors have given approval to the final version of the manuscript. [+]These authors contributed equally.

Notes

The authors declare no competing financial interests.

ACKNOWLEDGMENT

This work was supported by the Research Grants Council of the Hong Kong Special Administrative Region, China (Project No. PolyU152140/19E), the Hong Kong Polytechnic University (Project Nos. Q54V and G-UABC), and National Natural Science Foundation of China (No. 11804286 and 11704291). The DFT calculations were partially performed on Apollo cluster at the Department of Applied Physics, the Hong Kong Polytechnic University. We thank Professor Kailun Yao from Huazhong University of Science and Technology for providing software support for NEGF calculations.

REFERENCES

1. Fujishima, A.; Honda, K., Electrochemical photolysis of water at a semiconductor electrode. *Nature* **1972**, *238*, 37.

2. Ran, J.; Zhang, J.; Yu, J.; Jaroniec, M.; Qiao, S. Z., Earth-abundant cocatalysts for semiconductor-based photocatalytic water splitting. *Chem. Soc. Rev.* **2014**, *43*, 7787-7812.

3. Tan, C.; Cao, X.; Wu, X. J.; He, Q.; Yang, J.; Zhang, X.; Chen, J.; Zhao, W.; Han, S.; Nam, G. H., et al., Recent Advances in Ultrathin Two-Dimensional Nanomaterials. *Chem. Rev.* **2017**, *117*, 6225-6331.

4. Kudo, A.; Miseki, Y., Heterogeneous photocatalyst materials for water splitting. *Chem. Soc. Rev.* **2009**, *38*, 253-278.

5. Chen, X.; Shen, S.; Guo, L.; Mao, S. S., Semiconductor-based photocatalytic hydrogen generation. *Chem. Rev.* **2010**, *110*, 6503-6570.

6. Singh, A. K.; Mathew, K.; Zhuang, H. L.; Hennig, R. G., Computational Screening of 2D Materials for Photocatalysis. *J. Phys. Chem. Lett.* **2015**, *6*, 1087-1098.

7. Qiao, M.; Liu, J.; Wang, Y.; Li, Y.; Chen, Z., $PdSeO_3$ Monolayer: Promising Inorganic 2D Photocatalyst for Direct Overall Water Splitting Without Using Sacrificial Reagents and Cocatalysts. *J. Am. Chem. Soc.* **2018**, *140*, 12256-12262.

8. Luo, B.; Liu, G.; Wang, L., Recent advances in 2D materials for photocatalysis. *Nanoscale* **2016**, *8*, 6904-6920.

9. Fu, C. F.; Wu, X.; Yang, J., Material Design for Photocatalytic Water Splitting from a Theoretical Perspective. *Adv. Mater.* **2018**, *30*, 1802106.

10. Zhang, X.; Zhao, X.; Wu, D.; Jing, Y.; Zhou, Z., $MnPSe_3$ Monolayer: A Promising 2D Visible-Light Photohydrolytic Catalyst with High Carrier Mobility. *Adv. Sci. (Weinh)* **2016**, *3*, 1600062.

11. Ji, Y.; Yang, M.; Dong, H.; Hou, T.; Wang, L.; Li, Y., Two-dimensional germanium monochalcogenide photocatalyst for water splitting under ultraviolet, visible to near-infrared light. *Nanoscale* **2017**, *9*, 8608-8615.

12. Qiao, M.; Chen, Y.; Wang, Y.; Li, Y., The germanium telluride monolayer: a two dimensional semiconductor with high carrier mobility for photocatalytic water splitting. *J. Mater. Chem. A* **2018**, *6*, 4119-4125.

13. Jing, Y.; Heine, T., Two-dimensional $Pd_3P_2S_8$ semiconductors as photocatalysts for the solar-driven oxygen evolution reaction: a theoretical investigation. *J. Mater. Chem. A* **2018**, *6*, 23495-23501.

14. Ma, X.; Wu, X.; Wang, H.; Wang, Y., A Janus MoSSe monolayer: a potential wide solar-spectrum water-splitting photocatalyst with a low carrier recombination rate. *J. Mater. Chem. A* **2018**, *6*, 2295-2301.

15. Guan, Z.; Ni, S.; Hu, S., Tunable Electronic and Optical Properties of Monolayer and Multilayer Janus MoSSe as a Photocatalyst for Solar Water Splitting: A First-Principles Study. *J. Phys. Chem. C* **2018**, *122*, 6209-6216.

16. Tang, C.; Zhang, C.; Matta, S. K.; Jiao, Y.; Ostrikov, K.; Liao, T.; Kou, L.; Du, A., Predicting New Two-Dimensional $Pd_3(PS_4)_2$ as an Efficient Photocatalyst for Water Splitting. *J. Phys. Chem. C* **2018**, *122*, 21927-21932.

17. Matta, S. K.; Zhang, C.; Jiao, Y.; O'Mullane, A.; Du, A., Versatile two-dimensional silicon diphosphide (SiP_2) for photocatalytic water splitting. *Nanoscale* **2018**, *10*, 6369-6374.

18. Peng, R.; Ma, Y.; Huang, B.; Dai, Y., Two-dimensional Janus PtSSe for photocatalytic water splitting under the visible or infrared light. *J. Mater. Chem. A* **2019**, *7*, 603-610.

19. Sun, S.; Meng, F.; Xu, Y.; He, J.; Ni, Y.; Wang, H., Flexible, auxetic and strain-tunable two dimensional penta-X_2C family as water splitting photocatalysts with high carrier mobility. *J. Mater. Chem. A* **2019**, *7*, 7791-7799.

20. Mounet, N.; Gibertini, M.; Schwaller, P.; Campi, D.; Merkys, A.; Marrazzo, A.; Sohier, T.; Castelli, I. E.; Cepellotti, A.; Pizzi, G., et al., Two-dimensional materials from high-throughput computational exfoliation of experimentally known compounds. *Nat. Nanotechnol.* **2018**, *13*, 246-252.

21. Heyd, J.; Peralta, J. E.; Scuseria, G. E.; Martin, R. L., Energy band gaps and lattice parameters evaluated with the Heyd-Scuseria-Ernzerhof screened hybrid functional. *J. Chem. Phys.* **2005**, *123*, 174101.

22. Köhler, J.; Urland, W., RhTeCl–das erste Chalkogenidhalogenid eines Platinmetalls mit Schichtstruktur. *Z. Anorg. Allg. Chem.* **1997**, *623*, 583-586.

23. Qu, H.; Guo, S.; Zhou, W.; Cai, B.; Zhang, S.; Huang, Y.; Li, Z.; Chen, X.; Zeng, H., Electronic structure and transport properties of 2D RhTeCl: a NEGF-DFT study. *Nanoscale* **2019**, *11*, 20461-20466.

24. Kresse, G.; Furthmüller, J., Efficient iterative schemes for ab initio total-energy calculations using a plane-wave basis set. *Phys. Rev. B* **1996**, *54*, 11169.

25. Kresse, G.; Joubert, D., From ultrasoft pseudopotentials to the projector augmented-wave method. *Phys. Rev. B* **1999**, *59*, 1758.

26. Perdew, J. P.; Burke, K.; Ernzerhof, M., Generalized gradient approximation made simple. *Phys. Rev. Lett.* **1996**, *77*, 3865.

27. Monkhorst, H. J.; Pack, J. D., Special points for Brillouin-zone integrations. *Phys. Rev. B* **1976**, *13*, 5188-5192.

28. Heyd, J.; Scuseria, G. E.; Ernzerhof, M., Hybrid functionals based on a screened Coulomb potential. *J. Chem. Phys.* **2003**, *118*, 8207-8215.

29. Krukau, A. V.; Vydrov, O. A.; Izmaylov, A. F.; Scuseria, G. E., Influence of the exchange screening parameter on the performance of screened hybrid functionals. *J. Chem. Phys.* **2006**, *125*, 224106.

30. Grimme, S.; Antony, J.; Ehrlich, S.; Krieg, H., A consistent and accurate ab initio parametrization of density functional dispersion correction (DFT-D) for the 94 elements H-Pu. *J. Chem. Phys.* **2010**, *132*, 154104.

31. Momma, K.; Izumi, F., VESTA 3 for three-dimensional visualization of crystal, volumetric and morphology data. *J. Appl. Crystallogr.* **2011**, *44*, 1272-1276.

32. Togo, A.; Tanaka, I., First principles phonon calculations in materials science. *Scr. Mater.* **2015**, *108*, 1-5.

33. Nosé, S., A unified formulation of the constant temperature molecular dynamics methods. *J. Chem. Phys.* **1984**, *81*, 511-519.

34. Hoover, W. G., Canonical dynamics: Equilibrium phase-space distributions. *Phys. Rev. A* **1985**, *31*, 1695-1697.

35. Taylor, J.; Guo, H.; Wang, J., Ab initio modeling of quantum transport properties of molecular electronic devices. *Phys. Rev. B* **2001**, *63*, 245407.

36. Brandbyge, M.; Mozos, J.-L.; Ordejón, P.; Taylor, J.; Stokbro, K., Density-functional method for nonequilibrium electron transport. *Phys. Rev. B* **2002**, *65*, 165401.

37. Soler, J. M.; Artacho, E.; Gale, J. D.; García, A.; Junquera, J.; Ordejón, P.; Sánchez-Portal, D., The SIESTA method forab initioorder-Nmaterials simulation. *J. Phys.: Condens. Matter* **2002**, *14*, 2745-2779.

38. Salpeter, E. E.; Bethe, H. A., A Relativistic Equation for Bound-State Problems. *Phys. Rev.* **1951**, *84*, 1232-1242.

39. Bickers, N. E.; Scalapino, D. J.; White, S. R., Conserving approximations for strongly correlated electron systems: Bethe-Salpeter equation and dynamics for the two-dimensional Hubbard model. *Phys. Rev. Lett.* **1989**, *62*, 961-964.

40. Dancoff, S. M., Non-Adiabatic Meson Theory of Nuclear Forces. *Phys. Rev.* **1950**, *78*, 382-385.

41. Peterson, A. A.; Abild-Pedersen, F.; Studt, F.; Rossmeisl, J.; Nørskov, J. K., How copper catalyzes the electroreduction of carbon dioxide into hydrocarbon fuels. *Energy Environ. Sci.* **2010**, *3*, 1311-1315.

42. Nørskov, J. K.; Rossmeisl, J.; Logadottir, A.; Lindqvist, L.; Kitchin, J. R.; Bligaard, T.; Jonsson, H., Origin of the overpotential for oxygen reduction at a fuel-cell cathode. *J. Phys. Chem. B* **2004**, *108*, 17886-17892.

43. Cahangirov, S.; Topsakal, M.; Akturk, E.; Sahin, H.; Ciraci, S., Two- and one-dimensional honeycomb structures of silicon and germanium. *Phys. Rev. Lett.* **2009**, *102*, 236804.

44. Şahin, H.; Cahangirov, S.; Topsakal, M.; Bekaroglu, E.; Akturk, E.; Senger, R. T.; Ciraci, S., Monolayer honeycomb structures of group-IV elements and III-V binary compounds: First-principles calculations. *Phys. Rev. B* **2009**, *80*, 155453.

45. Blonsky, M. N.; Zhuang, H. L.; Singh, A. K.; Hennig, R. G., Ab initio prediction of piezoelectricity in two-dimensional materials. *ACS Nano* **2015**, *9*, 9885-9891.

46. Le Page, Y.; Saxe, P., Symmetry-general least-squares extraction of elastic data for strained materials fromab initiocalculations of stress. *Phys. Rev. B* **2002**, *65*, 104104.

47. Andrew, R. C.; Mapasha, R. E.; Ukpong, A. M.; Chetty, N., Mechanical properties of graphene and boronitrene. *Phys. Rev. B* **2012**, *85*, 125428.

48. Mouhat, F.; Coudert, F.-X., Necessary and sufficient elastic stability conditions in various crystal systems. *Phys. Rev. B* **2014**, *90*, 224104.

49. Cadelano, E.; Palla, P. L.; Giordano, S.; Colombo, L., Elastic properties of hydrogenated graphene. *Phys. Rev. B* **2010**, *82*, 235414.

50. Wang, L.; Kutana, A.; Zou, X.; Yakobson, B. I., Electro-mechanical anisotropy of phosphorene. *Nanoscale* **2015**, *7*, 9746-9751.

51. Cooper, R. C.; Lee, C.; Marianetti, C. A.; Wei, X.; Hone, J.; Kysar, J. W., Nonlinear elastic behavior of two-dimensional molybdenum disulfide. *Phys. Rev. B* **2013**, *87*, 035423.

52. Novoselov, K. S.; Jiang, D.; Schedin, F.; Booth, T.; Khotkevich, V.; Morozov, S.; Geim, A. K., Two-dimensional atomic crystals. *Proc. Natl. Acad. Sci. U. S. A.* **2005**, *102*, 10451-10453.

53. Mak, K. F.; Lee, C.; Hone, J.; Shan, J.; Heinz, T. F., Atomically thin MoS_2: a new direct-gap semiconductor. *Phys. Rev. Lett.* **2010**, *105*, 136805.

54. Butler, S. Z.; Hollen, S. M.; Cao, L.; Cui, Y.; Gupta, J. A.; Gutiérrez, H. R.; Heinz, T. F.; Hong, S. S.; Huang, J.; Ismach, A. F., Progress, challenges, and opportunities in two-dimensional materials beyond graphene. *ACS Nano* **2013**, *7*, 2898-2926.

55. Zacharia, R.; Ulbricht, H.; Hertel, T., Interlayer cohesive energy of graphite from thermal desorption of polyaromatic hydrocarbons. *Phys. Rev. B* **2004**, *69*, 155406.

56. Li, F.; Liu, X.; Wang, Y.; Li, Y., Germanium monosulfide monolayer: a novel two-dimensional semiconductor with a high carrier mobility. *J. Mater. Chem. C* **2016**, *4*, 2155-2159.

57. Vaughn, D. D.; Patel, R. J.; Hickner, M. A.; Schaak, R. E., Single-crystal colloidal nanosheets of GeS and GeSe. *J. Am. Chem. Soc.* **2010**, *132*, 15170-15172.

58. Zhao, S.; Li, Z.; Yang, J., Obtaining two-dimensional electron gas in free space without resorting to electron doping: an electride based design. *J. Am. Chem. Soc.* **2014**, *136*, 13313-13318.

59. Druffel, D. L.; Kuntz, K. L.; Woomer, A. H.; Alcorn, F. M.; Hu, J.; Donley, C. L.; Warren, S. C., Experimental Demonstration of an Electride as a 2D Material. *J. Am. Chem. Soc.* **2016**, *138*, 16089-16094.

60. Hua, C.; Sheng, F.; Hu, Q.; Xu, Z. A.; Lu, Y.; Zheng, Y., Dialkali-Metal Monochalcogenide Semiconductors with High Mobility and Tunable Magnetism. *J. Phys. Chem. Lett.* **2018**, *9*, 6695-6701.

61. Zhang, S.; Wang, Q.; Kawazoe, Y.; Jena, P., Three-dimensional metallic boron nitride. *J. Am. Chem. Soc.* **2013**, *135*, 18216-18221.

62. Bardeen, J.; Shockley, W., Deformation potentials and mobilities in non-polar crystals. *Phys. Rev.* **1950**, *80*, 72.

63. Cai, Y.; Zhang, G.; Zhang, Y. W., Polarity-reversed robust carrier mobility in monolayer MoS_2 nanoribbons. *J. Am. Chem. Soc.* **2014**, *136*, 6269-6275.

64. Albrecht, S.; Reining, L.; Del Sole, R.; Onida, G., Ab initio calculation of excitonic effects in the optical spectra of semiconductors. *Phys. Rev. Lett.* **1998**, *80*, 4510.

65. Rohlfing, M.; Louie, S. G., Electron-hole excitations and optical spectra from first principles. *Phys. Rev. B* **2000**, *62*, 4927.

66. Shirayama, M.; Kadowaki, H.; Miyadera, T.; Sugita, T.; Tamakoshi, M.; Kato, M.; Fujiseki, T.; Murata, D.; Hara, S.; Murakami, T. N., Optical transitions in hybrid perovskite solar cells: ellipsometry, density functional theory, and quantum efficiency analyses for $CH_3NH_3PbI_3$. *Phys. Rev. Appl.* **2016**, *5*, 014012.

67. Bajdich, M.; Garcia-Mota, M.; Vojvodic, A.; Norskov, J. K.; Bell, A. T., Theoretical investigation of the activity of cobalt oxides for the electrochemical oxidation of water. *J. Am. Chem. Soc.* **2013**, *135*, 13521-13530.

68. Zhang, X.; Chen, A.; Zhang, Z.; Jiao, M.; Zhou, Z., Transition metal anchored C_2N monolayers as efficient bifunctional electrocatalysts for hydrogen and oxygen evolution reactions. *J. Mater. Chem. A* **2018**, *6*, 11446-11452.